Particle
& Particle Systems Characterization
www.particle-journal.com
Materials Views
www.MaterialsViews.com

A Multifunctional Magnetic Composite Material as a Drug Delivery System and a Magnetic Resonance Contrast Agent

Guilong Zhang, Junlan Gao, Junchao Qian, Dongqing Cai, Kang Zheng, Zhiwu Yu, Junfeng Wang, Kai Zhong, Xin Zhang,* and Zhengyan Wu**

Magnetic iron oxide coated in hydrogenation silica (Fe_3O_4@$HSiO_2$) is constructed as both a tumor drug carrier and a magnetic resonance (MR) contrast agent. Colchicine (COLC) is loaded in Fe_3O_4@$HSiO_2$ with the highest amount of 28.3 wt% at pH 9. The release performance of COLC can be controlled by pH, as the porous $HSiO_2$ shell can partially shed at pH below 3.0 to facilitate the release of COLC. MR imaging (MRI) tests prove that Fe_3O_4@$HSiO_2$ at pH 3.0 (H^+-Fe_3O_4@$HSiO_2$) shows a stronger MR contrast enhancement than Fe_3O_4. Cytotoxicity experiment indicates that Fe_3O_4@$HSiO_2$ has excellent biocompatibility and magnetic targeting performance. Additionally, COLC-loaded Fe_3O_4@$HSiO_2$ (Fe_3O_4@$HSiO_2$–COLC) displays a higher inhibition effect on tumor cells under a magnetic field than free COLC. The visibility upon MRI, high targeting, and pH-controlled release characteristics of Fe_3O_4@$HSiO_2$–COLC are favorable to achieve the aim of reducing side effects to normal tissues, making Fe_3O_4@$HSiO_2$–COLC an attractive drug delivery system for nanomedicine.

1. Introduction

The clinical use of a great many anticancer drugs is currently limited due to their poor ability to permeate into tumor tissue and side effects on healthy cells, which also limit the dose of drug that can be safely administrated to cancer patients.[1] Fabrication of anticancer nanomedicine with high delivery specificity, controllable release, and diagnostic visibility has been considered as a promising approach to resolve these problems,[2,3] wherein a great progress has been achieved in the past few years.[4–7]

Anticancer nanodrug with high delivery specificity (actually targeted delivery) could be obtained through loading the drugs onto nanostructured lipid carrier noted by antibody[8] or nanostructured magnetic materials that could deliver the drugs to the target tumor under magnetic field.[9,10] However, some barriers still exist to attenuate the penetration rate of drug molecules from the bloodstream to disease tissue so that the drug molecules can be easily filtered by kidney or prematurely cleared by the reticuloendothelial system (RES).[11,12] To solve these problems, functional magnetic nanomaterials that could increase the circulating half-life of the particles as well as their biodistribution have been widely investigated in targeted drug delivery systems due to the nontoxicity, ideal homogeneous size, and excellent biocompatibility.

Controlled release is another important factor for anticancer nanomedicine, as it could maintain the critical concentration of drugs in diseased tissue and thus enhance treatment efficiency and decrease drug toxicity for normal cell.[13] It is well known that ordered porous silica owns stable structure,[14,15] large surface area, and high biocompatibility[16] and is suitable to be used as a drug controlled release carrier. Normally, the controlled release performance of nanomedicine based on ordered porous silica can be adjusted through pH,[17] light,[18] and temperature.[19,20]

Besides the high targeted delivery and controlled release properties mentioned above, the visibility in vivo is another key factor for the anticancer nanodrug to trace the prognosis of the tumor. Magnetic iron oxide (MIO), as an ideal negative contrast agent, is attracting more and more interests. MIO nanoparticles cause local inhomogeneities in the magnetic field, resulting in further decoherence of the water proton precession of the spins. Typically, MIO contrast agents are composed of an MIO core and a polymer or polysaccharide shell,[21] which can decrease mainly transverse relaxation time (T_2) of the water molecules surrounding the nanoparticles in magnetic resonance imaging

G. Zhang, Dr. D. Cai, Prof. Z. Wu
Key Laboratory of Ion Beam Bioengineering
Hefei Institutes of Physical Science
Chinese Academy of Sciences
Hefei 230031, People's Republic of China
E-mail: zywu@ipp.ac.cn
G. Zhang
University of Science and Technology of China
Hefei 230026, People's Republic of China
J. Gao, Prof. X. Zhang
School of Life Sciences
Anhui Agricultural University
Hefei 230036, People's Republic of China
E-mail: xinzhang@ahau.edu.cn
Dr. J. Qian, Dr. Z. Yu, Prof. J. Wang, Prof. K. Zhong
High Magnetic Field Laboratory
Hefei Institutes of Physical Science
Chinese Academy of Sciences
Hefei 230031, People's Republic of China
E-mail: kzhong@hmfl.ac.cn
Dr. K. Zheng
Key Laboratory of Materials Physics
Institute of Solid State Physics
Chinese Academy of Sciences
Hefei 230031, People's Republic of China

DOI: 10.1002/ppsc.201300366

(MRI). The reduced transverse relaxation time of spins causes a negative contrast in the bright MR image.[2] Thus, diseased tissue with different T_2 can be easily detected. As a contrast agent, MIO has been extensively investigated for a better medicine diagnosis.[22]

Although research on nanodrug with high delivery specificity, controllable release, and visibility has been widely investigated and gained huge progress, there are still some disadvantages including the low loading ability of drug, poor release controllability, and premature contrast agent. Low loading amount of drug will result in the insufficient drug concentration in the tumor tissue and thus low therapeutic effect.[23] Bad controllability of drug release tends to cause a burst release, which can lead to a toxicity risk for normal cells.[24,25] Use of premature contrast agent will make the imaging in vivo unstable and low contrast. Gao et al. described a drug carrier and contrast agent prepared by polymeric micelles containing MIO.[26,27] This work could make delivering anticancer drug to specific tumor tissue and monitoring variation of tumor available. However, as Chen et al. described, the intrinsic unstable nature of such organic system in vivo still casts a shadow on their further clinical use.[28]

In this article, we synthesized a new tumor drug carrier and magnetic resonance (MR) contrast agent using MIO coated by hydrogenation silica (designated as Fe_3O_4@$HSiO_2$) that showed excellent stability in simulated body fluid (SBF). Colchicine (COLC) was chosen as the model tumor drug, which was loaded in Fe_3O_4@$HSiO_2$ (designated as Fe_3O_4@$HSiO_2$–COLC). Compared with previously reported nanodrug,[29,30] Fe_3O_4@$HSiO_2$–COLC displayed accurate targeting, high drug-loading amount, pH-controllable release, strong contrast enhancement, and outstanding permeability under the magnetic field. Moreover, cytotoxicity experiment demonstrated that Fe_3O_4@$HSiO_2$–COLC possessed an excellent inhibitory effect on HepG2 cells. This work provides a promising and facile approach to fabricate a system acting as both drug carrier and MR contrast agent, which could target a specific tumor tissue to release anticancer drug, and meanwhile monitor the tumor treatment by MRI. Therefore, this system could have a potential application in cancer therapy and diagnosis.

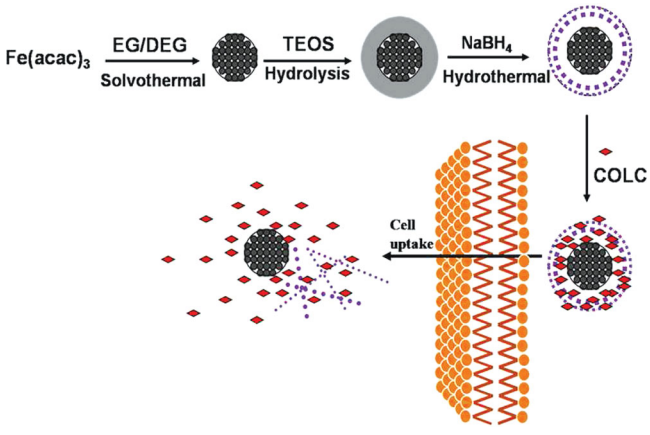

Scheme 1. A graphical representation of the fabrication of porous Fe_3O_4@$HSiO_2$ core–shell nanoparticles and a drug release process.

2. Results and Discussion

2.1. Materials Analysis

The fabrication of porous Fe_3O_4@$HSiO_2$ nanospheres was outlined in **Scheme 1**. Homogeneous Fe_3O_4 nanospheres with diameter of about 100 nm were synthesized through a solvothermal method, as shown in **Figure 1**a,b. From a high-resolution TEM (HRTEM) image of a single Fe_3O_4 nanosphere (Figure 1c), it could be seen that a nanosphere seemed to be composed of lots of tiny nanocrystals with a size of about 5 nm. Lattice fringes were recorded for the Fe_3O_4 nanosphere, and the distance between two adjacent planes of a tiny nanocrystal was measured to be 0.294 nm, corresponding to (220) planes in the spinel-structured Fe_3O_4 (Figure 1c). The selected-area electron diffraction (SAED) pattern of Fe_3O_4 nanocluster was recorded and displayed polycrystal-line-like diffraction, which indicated that nanocluster was formed from small magnetic Fe_3O_4 nanocrystals (Figure 1d).

After that, the Fe_3O_4@SiO_2 core–shell nanoparticle was synthesized from monodispersed Fe_3O_4 nanocrystal (≈100 nm diameter) as a core and tetraethyl orthosilicate (TEOS) as a silica source by the Stöber method.[31] By carefully controlling the hydrolysis conditions, uniform Fe_3O_4@SiO_2 core–shell nanoparticles with diameter ≈180 nm were formed in this process, and each nanoparticle owned a 40-nm-thick shell, as shown in **Figure 2**a,b. Consequently, porous Fe_3O_4@$HSiO_2$ core–shell nanoparticles were gained through the reduction of Fe_3O_4@SiO_2 core–shell nanoparticles. Particle size distribution of Fe_3O_4@$HSiO_2$ was determined by dynamic light scattering (DLS). As shown in Figure S1 (Supporting Information), the average size of Fe_3O_4@$HSiO_2$ was 206 nm, larger than the size shown in transmission electron microscopy (TEM). This is due to the aggregation of some nanoparticles. From Figure 2c, it could be seen clearly that, compared with Fe_3O_4@SiO_2, the shell of Fe_3O_4@$HSiO_2$ was much thinner and looser, which implied that the nest-like porous SiO_2 shell formed after the hydrothermal reduction (inset of Figure 2c). This process could be that $NaBH_4$ first dissolved external silica into monosilicate making silicate supersaturated around the particles, which induced the internal silica to join in the regrowth of silica shell, and porous $HSiO_2$ shell eventually formed, this could be explained by the Ostwald ripening mechanism.[32]

In order to investigate the mechanism of the porous shell formed, proton magnetic resonance (HNMR) and FTIR analysis of Fe_3O_4@SiO_2 and Fe_3O_4@$HSiO_2$ were performed. The peaks at 1635 and 3415 cm^{-1} found in the FTIR spectra were assigned to Si — O—H bending and stretching vibrations. Compared with Fe_3O_4@SiO_2, a great many of silanol groups were formed in the porous shell of Fe_3O_4@$HSiO_2$ (Figure S2, Supporting Information), and this could also be demonstrated from HNMR spectra (**Figure 3**). Signals at 6.3 and 5.3 could be attributed to H_2O absorbed on bridged hydroxyls. Signals at 3.5 and 3.7 could be be ascribed to physisorbed H_2O. Signal at 2.1 could be assigned to the terminal silanol on Fe_3O_4@SiO_2 nanosphere. Signal at 1.2 could be assigned to the silanol because of oxygen vacancies in Fe_3O_4@$HSiO_2$ nanosphere.[33] Compared with Fe_3O_4@SiO_2, it was found that in Fe_3O_4@$HSiO_2$ a new strong peak at 1.2 appeared and meanwhile signal at 2.1

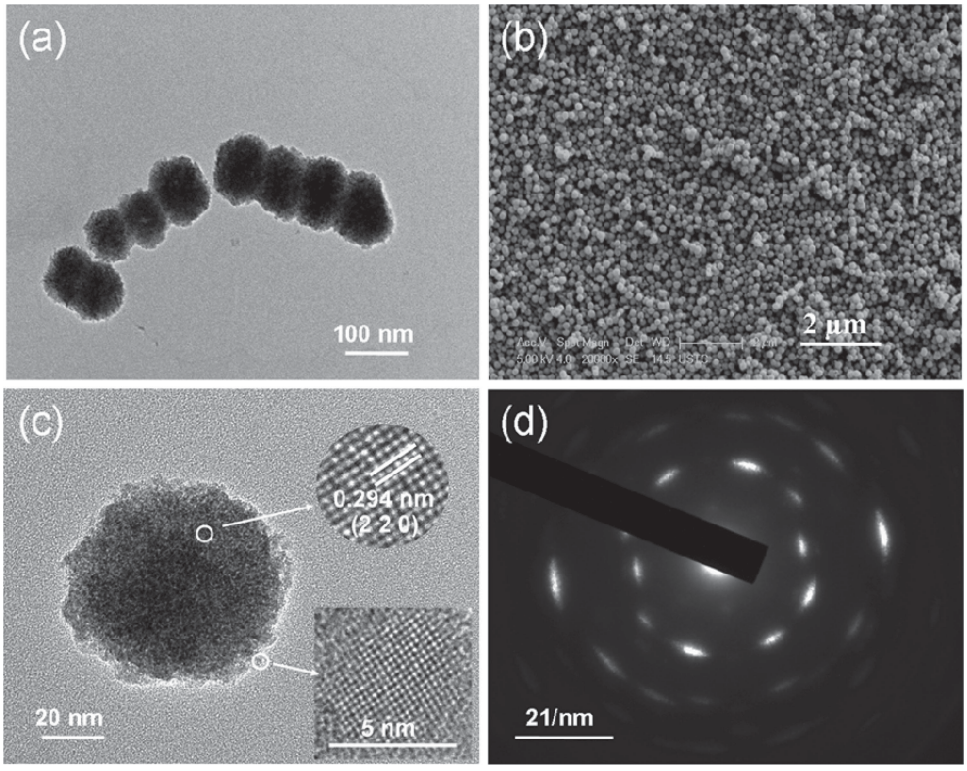

Figure 1. a) TEM and b) SEM images of Fe_3O_4; c) HRTEM image of an 80 nm Fe_3O_4 cluster; d) SAED pattern of the cluster in (c).

disappeared, which means the terminal silanol disappeared, indicating oxygen vacancies formed in Fe_3O_4@$HSiO_2$. Furthermore, the amounts of silanols resulting from oxygen vacancies were five times the amounts of original terminal silanols by a integral calculation. Additionally, the disappearance of terminal silanols could imply that the nest-like porous shell of Fe_3O_4@

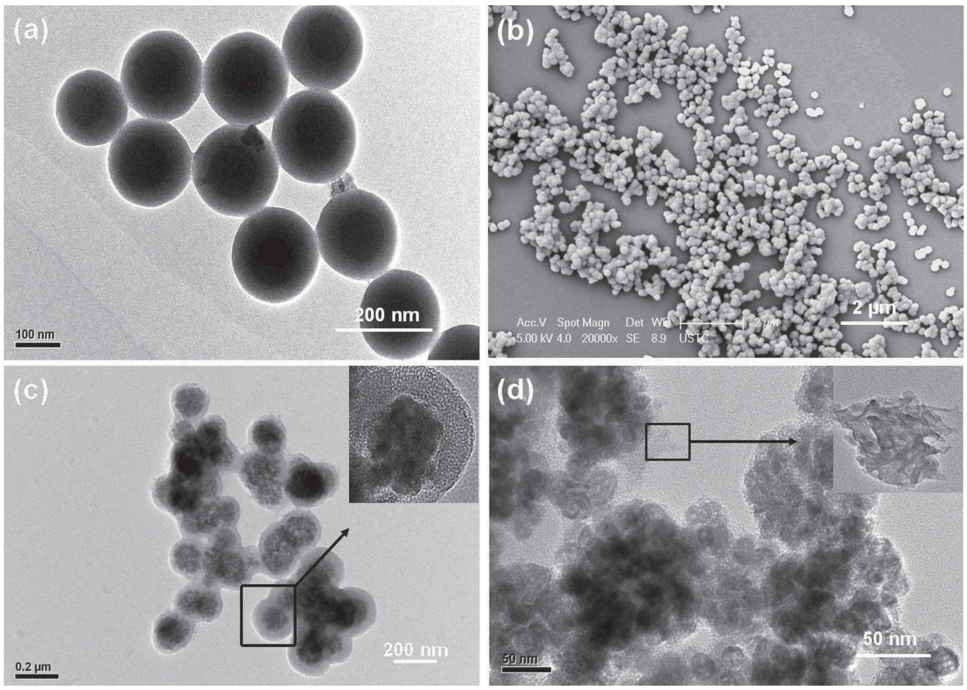

Figure 2. a) TEM and b) SEM images of Fe_3O_4@SiO_2; TEM images of c) Fe_3O_4@$HSiO_2$ and d) H^+-Fe_3O_4@$HSiO_2$ (inset of (c, d): the amplified image of the square region and circle region, respectively).

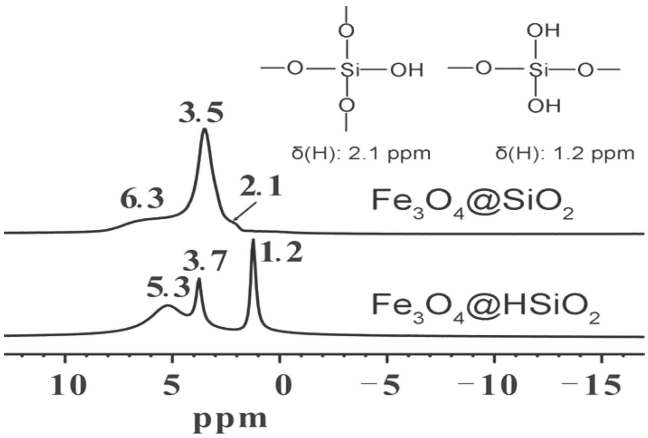

Figure 3. HNMR spectra of Fe_3O_4@SiO_2 and Fe_3O_4@$HSiO_2$.

$HSiO_2$ was formed by the oxygen vacancies silanols linkages (Figure S3, Supporting Information).

In addition, from Figure 2d, it could be seen that the porous shell shed partially from the Fe_3O_4@$HSiO_2$ core–shell nanoparticles at pH < 3.0 (designated as H^+-Fe_3O_4@$HSiO_2$) so that a great number of rough silica slices appeared (seen in inset of Figure 2d). Average size of H^+-Fe_3O_4@$HSiO_2$ (120 nm) obtained from DLS analysis (Figure S1, Supporting Information) also demonstrated the shedding of nest-like porous shell. We also investigated the shell's shedding by zeta potential test (Figure S4, Supporting Information). Fe_3O_4@$HSiO_2$ showed more negative values compared with Fe_3O_4@SiO_2 in neutral solution because more silanol groups formed. For pH lower than 4.0, zeta potentials of Fe_3O_4@SiO_2 and Fe_3O_4@$HSiO_2$ both showed positive values, which is due to protonation of silanol groups. Furthermore, the zeta potential of Fe_3O_4@$HSiO_2$ increased faster than that of Fe_3O_4@SiO_2 with decreasing pH. Therefore, it could be concluded that the electrostatic repulsion between silanols linkages led to the nest-like porous shell shedding easily under acidic conditions.

As we known, the silica nanospheres obtained through the typical Stöber process possess micropores structure. The nitrogen adsorption–desorption isotherm of Fe_3O_4@$HSiO_2$ and Fe_3O_4@SiO_2 and their pore size distribution (PSD) curves were investigated and shown in Figure S5 (Supporting Information). The isotherm of Fe_3O_4@SiO_2 exhibited low absorption capacity, and indicated that nanospheres possessed low porosity. The corresponding PSD showed that nanospheres possessed micropores structure, but the porosity was low. The isotherm of Fe_3O_4@$HSiO_2$ by hydrogenation exhibited that the nanospheres possessed a mesoporous structure. The corresponding PSD indicated that the pore sizes mainly distributed at 2.2 and 5.7 nm. In addition, COLC molecule size was simulated by Chemdraw software to be around 1.36 nm (Figure S6, Supporting Information), suggesting that COLC molecules could be well loaded into porous Fe_3O_4@$HSiO_2$.

2.2. Magnetic Property Investigation

The magnetic properties of the nanoparticles were investigated using a vibrating sample magnetometer. Hysteresis loop implied

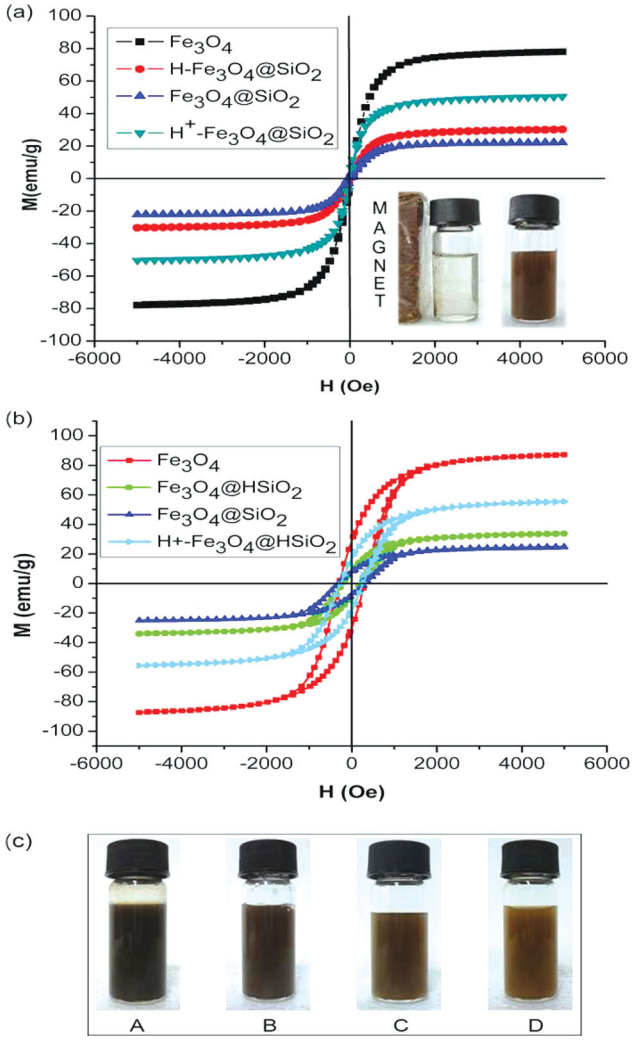

Figure 4. Hysteresis loops of samples at a) 300 K and b) 3 K. c) Suspension of samples: A) Fe_3O_4, B) Fe_3O_4@$HSiO_2$, C) Fe_3O_4@SiO_2, and D) H^+-Fe_3O_4@$HSiO_2$ (insets of (a): (left) Fe_3O_4@$HSiO_2$ subjected to applied magnetic field, (right) Fe_3O_4@$HSiO_2$ not subjected to applied magnetic field).

the sample's response ability to an externally applied magnetic field (inset of **Figure 4**a). Magnetic measurement showed that all the samples (Fe_3O_4, Fe_3O_4@SiO_2, Fe_3O_4@$HSiO_2$, and H^+-Fe_3O_4@$HSiO_2$) possessed soft ferromagnetic due to the lack of coercive force and remanence at room temperature, seen in Figure 4a. Nevertheless, the soft ferromagnetic disappeared at 3 K and all the samples displayed typical ferromagnetic with coercivity (Hc = 346, 215, 350, 293 Oe), remanence (Mr = 27.5, 7.9, 7.5, and 16.2 emu g^{-1}) and higher saturated magnetization (Ms) values (87.3, 24.5, 33.8, and 55.6 emu g^{-1}) for Fe_3O_4, Fe_3O_4@SiO_2, Fe_3O_4@$HSiO_2$, and H^+-Fe_3O_4@$HSiO_2$, respectively (Figure 4b), this could be because the thermal energy at 3 K is too low to induce moment randomization.[34] In addition, Ms values showed that the magnetic response ability order (high to low) of the four samples was Fe_3O_4, H^+-Fe_3O_4@$HSiO_2$, Fe_3O_4@$HSiO_2$, and Fe_3O_4@SiO_2 at both 300 K and 3 K. Owing to the existence of SiO_2 coating, the proportion of Fe_3O_4

in Fe_3O_4@SiO_2 was lower than that in Fe_3O_4 alone. After reduction, the SiO_2 coating became thinner and looser, resulting in a higher proportion of Fe_3O_4 in Fe_3O_4@$HSiO_2$ than that in Fe_3O_4@SiO_2. In addition, under acidic condition, part of the SiO_2 shell would shed from the Fe_3O_4@$HSiO_2$ particles so that the proportion of Fe_3O_4 further increased. Correspondingly, the order (high to low) of the proportion of Fe_3O_4 in the four samples was consistent to that of magnetic response ability. Obviously, the magnetic response ability of the samples depended on their Fe_3O_4 content. As shown in Figure 4c, the color of these samples (Fe_3O_4, Fe_3O_4@$HSiO_2$, Fe_3O_4@SiO_2, and H^+-Fe_3O_4@$HSiO_2$) varied gradually from black to yellow, which was probably due to the crystal morphology transformation.

2.3. MRI Investigation

To investigate the MR contrast potential of Fe_3O_4, Fe_3O_4@$HSiO_2$, and H^+-Fe_3O_4@$HSiO_2$ nanoparticles, we measured the transverse relaxation (T_2) rate and calculated relaxivity. Proton relaxivity is the ratio of proton relaxation ($1/T_2$) to iron atom concentration. After the simple surface modification of the nanoparticles by sodium alginate, these three types of nanoparticles dispersed very well in water and kept an excellent stability, which could be because the surface of sodium-alginate-encapsulated magnetic nanoparticles was hydrophilic. To compare the MR apparent transverse relaxivities (r_2) of these magnetic nanoparticles, multi-echo spin echo images (TR (repetition time) 2.5 s with TEs (echo times) of 10–200 ms) for each sample were collected on a 14.1T MR microimaging system. As shown in **Figure 5**a, the Fe_3O_4 nanoparticles exhibited well MR signal attenuation effect with increasing concentrations of nanoparticles. However, Fe_3O_4@$HSiO_2$ core–shell nanoparticles exhibited a very poor MR contrast enhancement effect. We postulated that the shell of Fe_3O_4@$HSiO_2$ nanoparticles hindered MIO nanoparticles' ability as an MR agent. Surprisingly, H^+-Fe_3O_4@$HSiO_2$ core–shell nanocrystals showed a stronger MR relaxation enhancement than Fe_3O_4. The reason could be that, when core Fe_3O_4 magnetic nanoparticles were collected after the $HSiO_2$ shell of H^+-Fe_3O_4@$HSiO_2$ shed at pH 3.0, residual silica in core Fe_3O_4 nanoparticles surface of H^+-Fe_3O_4@$HSiO_2$ increased the dispersibility of nanoparticles so that the contact area with water could be increased. Additionally, from TEM image in Figure S7 (Supporting Information), it could be found that Fe_3O_4 nanospheres split into many tiny crystals, which also increased magnetic crystal's contact area with water. To verify this, the standard zero-field-cooling and field-cooling (ZFC/FC) curves of H^+-Fe_3O_4@$HSiO_2$ and Fe_3O_4 were obtained (Figure S8, Supporting Information). Compared with Fe_3O_4, the ZFC curve of H^+-Fe_3O_4@$HSiO_2$ appeared a new peak of lower blocking temperature (≈260 K), which indicated that Fe_3O_4 nanospheres split partially into smaller nanoparticles. Wherein crystal morphology change of core Fe_3O_4 could result in a stronger MR relaxation enhancement. So controlling the magnetic spins by changing the morphology of the nanoparticles could be critical for modulating the spin–spin relaxation processes of protons in the water molecules surrounding the nanoparticles, especially for solid nanoparticles.[35] Relaxivity (r_2) was used to estimate the MR contrast enhancement for

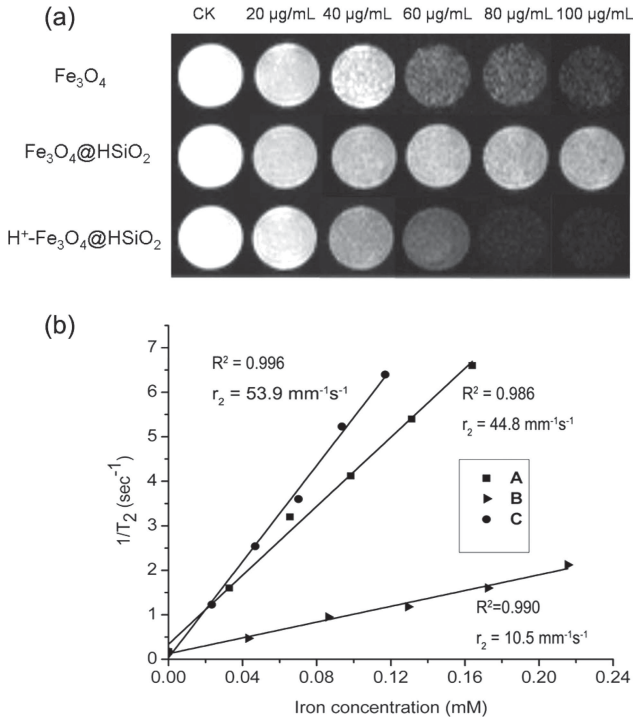

Figure 5. a) T_2-weighted MR images of Fe_3O_4, Fe_3O_4@$HSiO_2$, and H^+-Fe_3O_4@$HSiO_2$ with different concentrations from a 9.4 T MRI system containing 1% sodium alginate gel. b) Measurements of r_2 relaxivity for A) Fe_3O_4, B) Fe_3O_4@$HSiO_2$, and C) H^+-Fe_3O_4@$HSiO_2$.

three samples (Fe_3O_4, Fe_3O_4@$HSiO_2$, and H^+-Fe_3O_4@$HSiO_2$ nanoparticles) (Figure 5b). The r_2 values were 44.8, 10.5, and 53.9 (mM^{-1} s^{-1}), respectively. Compared with the other two samples, H^+-Fe_3O_4@$HSiO_2$ core–shell nanoparticles showed much a stronger MR contrast enhancement. Meanwhile, the relaxivity of H^+-Fe_3O_4@$HSiO_2$ was stronger than that of several routine MIO particles including crosslinked iron oxide (CLIO),[36] ferumoxtran,[37] and monocrystalline iron oxide nanoparticles (MION-46),[38] which implied that such Fe_3O_4@$HSiO_2$ could be used as a potential MR contrast agent to detect cancer.

Considering the excellent transverse relaxivity of H^+-Fe_3O_4@$HSiO_2$, we estimated further its MR contrast enhancement on HepG2 cells. The MR images of HepG2 cells incubated with different concentrations of iron (0, 20, 40, and 60 μg mL^{-1}) at 0 and 0.5 Tesla magnetic field were shown as **Figure 6**. Rapid and efficient magnetic targeting significantly darkened the MR images at 0.5 Tesla magnetic field compared with non-magnetic field (Figure 6a). In addition, the T_2 values of the solutions of HepG2 cells containing different concentrations of iron were evaluated. At 40 μg mL^{-1}, T_2 values decreased from 50 ms at non-magnetic field to 30 ms at 0.5 Tesla magnetic field (Figure 6b). Further decreases of T_2 values were observed at the higher iron concentrations at both 0 and 0.5 Tesla magnetic fields.

2.4. Loading and Release Behaviors of Fe_3O_4@$HSiO_2$–COLC

In order to obtain the potential of Fe_3O_4@$HSiO_2$ as a drug delivery system, its loading capacity and release behavior for

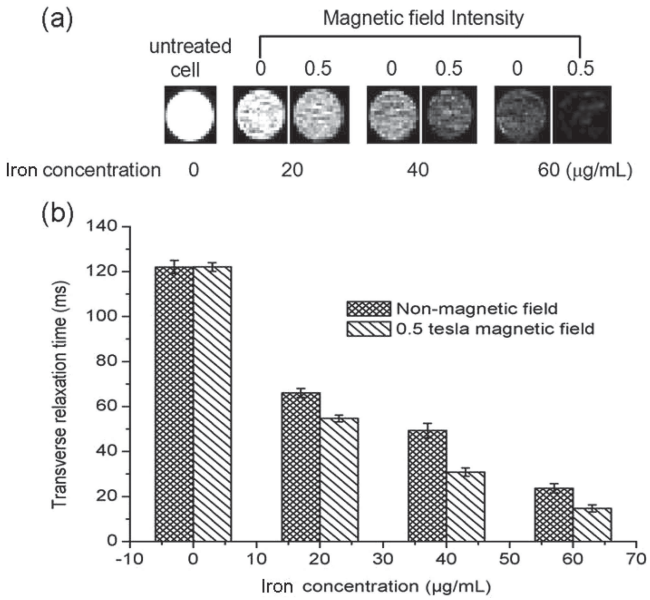

Figure 6. a) T_2-weighted images (9.4 T) and b) corresponding T_2 values of the solutions of untreated HepG2 cells, and HepG2 cells treated with different concentrations of iron (20, 40, and 60 μg mL^{-1}) at 0 and 0.5 Tesla magnetic field.

COLC were investigated. The result indicated that COLC could easily be loaded into Fe_3O_4@$HSiO_2$ with the highest loading amount of 28.3 wt% at pH 9.0. This was probably because, at alkaline condition, the —CONH— groups on COLC was deprotonated to form negative ion groups, which tended to bind to —SiOH on the shell of Fe_3O_4@$HSiO_2$ through hydrogen bonds and electrostatic forces (Figure S9a, Supporting Information). This was verified by FTIR analysis in Figure S9b (Supporting Information) wherein the C=O stretching vibration (1676 cm^{-1}) of —CONH— and the C—H stretching vibration (2937 cm^{-1}) of CH_3CONH— for COLC red-shifted to 1662 cm^{-1} and 2926 cm^{-1}, respectively, after being loaded in Fe_3O_4@$HSiO_2$. As shown in Figure S9c (Supporting Information), with the decreasing pH from 7.4 to 3.0, the release velocity of COLC increased and thus the equilibrium time shortened. The reason was probably that the SiO_2 shell of Fe_3O_4@$HSiO_2$ was easier to shed under low pH condition, which could facilitate the release of the COLC. In addition, under acidic condition, the hydrogen bonds between —CONH— and —SiOH tended to break, which was also favorable for the release of COLC. Such fast release property at low pH values made Fe_3O_4@$HSiO_2$–COLC suitable to be potential anticancer drug because of the suitable acidic microenvironment (approximately pH 4.0–4.5) in lysosomes of tumor cell.[18] Therefore, the anticancer drug could be targetedly delivered to tumor tissue and then release so that the damage of COLC to normal tissue cells could be effectively reduced.

2.5. Cell Assay

HepG2 was used to evaluate the in vitro cytotoxicity of free COLC, Fe_3O_4@$HSiO_2$, and Fe_3O_4@$HSiO_2$–COLC by CCK-8 assay. Cells exposed to COLC as a positive control showed an excellent inhibitory effect since COLC is a hydrophilic anticancer drug (**Figure 7**a-C), while Fe_3O_4@$HSiO_2$ nanoparticles did not show any cytotoxicity against HepG2 cells (Figure 7a-A), which indicated these particles had excellent biocompatibility. However, the Fe_3O_4@$HSiO_2$–COLC nanoparticles induced cell death was found to be dose-dependent and the phenomena were similar as COLC treatment after a 24 h incubation period (Figure 7a-B), which implied that COLC molecules could successfully release from the pore of Fe_3O_4@$HSiO_2$–COLC to the cancer cells to effective concentrations. These results were consistent with expectations.

To demonstrate the uptake of the Fe_3O_4@$HSiO_2$ nanoparticle for tumor cells, the cytotoxicity of the Fe_3O_4@$HSiO_2$–COLC not subjected to and subjected to magnetic field was investigated (Figure 7a-B and a-D). Compared with that not subjected

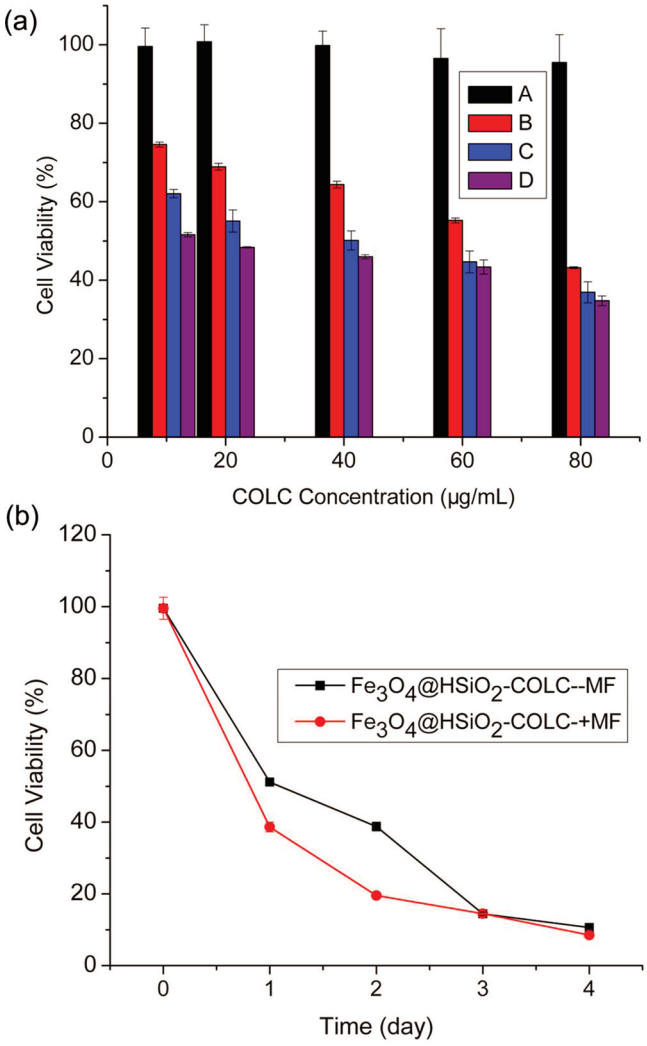

Figure 7. a) HepG2 cell viabilities measured by CCK-8 assay for an incubation period 24 h treated with different concentrations of A) Fe_3O_4@$HSiO_2$, B) Fe_3O_4@$HSiO_2$–COLC, C) free COLC, and D) Fe_3O_4@$HSiO_2$–COLC subjected to magnetic field at 0.5 Tesla. b) HepG2 cell viabilities with time treated with Fe_3O_4@$HSiO_2$–COLC subjected to magnetic field (+MF) at 0.5 Tesla and not subjected to magnetic field (–MF).

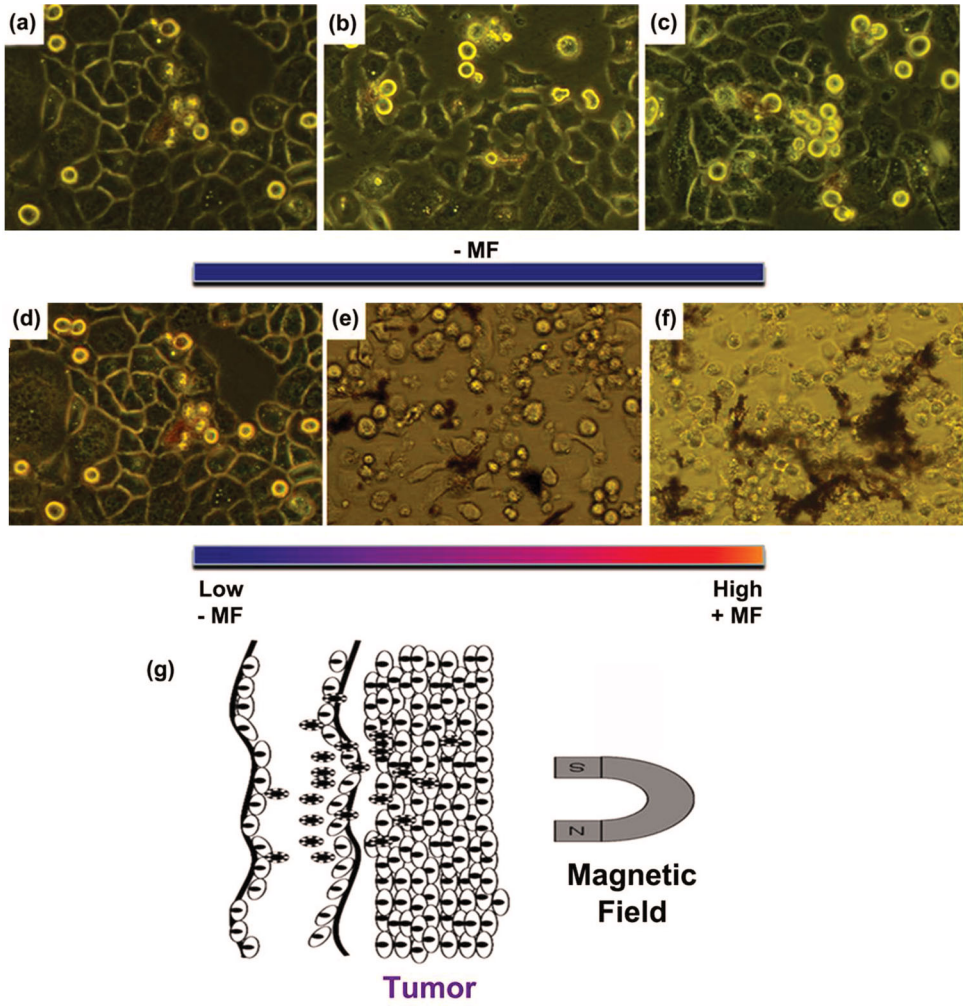

Figure 8. Morphology images of the incubated HepG2 cells (2×10^5 cells/dish) treated with 40 μg mL^{-1} Fe_3O_4@$HSiO_2$–COLC: a–c) not subjected to the magnetic field (-MF), subjected to the magnetic field (+MF) at d) 0.05 d), e) 0.15, and f) 0.5 Tesla for 24 h and defined by Fe_3O_4@$HSiO_2$ intensity increased with magnetic field treatment. Representative images are shown. Original magnification, ×200. g) Graphical representation of how porous magnetic materials delivered drug to special tissue under applied magnetic field.

to the magnetic field, all concentrations (10, 20, 40, 60, and 80 μg mL^{-1}) of Fe_3O_4@$HSiO_2$–COLC subjected to external magnetic field exhibited higher cytotoxicity. The cell viability decreased with the increasing incubation time (Figure 7b). After 2 d, few survived cells could be observed by microscope when the cells were treated with 40 μg mL^{-1} of Fe_3O_4@$HSiO_2$–COLC under an external magnetic field. These results implied that the magnetic field could increase the ability of Fe_3O_4@$HSiO_2$ nanoparticles to enter the tumor tissue and facilitate COLC killing the tumor cells more effectively.

To illustrate the effect of Fe_3O_4@$HSiO_2$–COLC on cells, the morphology images of HepG2 cells treated with free COLC and Fe_3O_4@$HSiO_2$–COLC (10, 40, and 80 μg mL^{-1}) for 24 h, subjected to and not subjected to magnetic field, were shown in Figure S10 (Supporting Information). Normally, HepG2 cells were attached the bottom of well before the treatment. After incubation with COLC or Fe_3O_4@$HSiO_2$–COLC, it was found the cell shape changed from flat to round, and the cell detached from the well bottom and floated in the media. The higher concentration of COLC or Fe_3O_4@$HSiO_2$–COLC, the more round-shape cells produced. When not subjected to magnetic field, only a few nanoparticles could be found around the cells, this could be because Fe_3O_4@$HSiO_2$–COLC were dispersed in culture media resulting in COLC molecules had few chance to reach cells (Figure S11b, Supporting Information). However, when subjected to magnetic field at 0.5 Tesla, Fe_3O_4@$HSiO_2$–COLC nanoparticles gathered to cytomembrane and were localized in the endosomes of HepG2 cells after cellular uptake (Figure S11a, Supporting Information),[17] which could increase more COLC on cytomembrane and probably promote the internalization of Fe_3O_4@$HSiO_2$–COLC in HepG2 cells.

To demonstrate the Fe_3O_4@$HSiO_2$–COLC nanoparticle's potential use as a targeted drug delivery system, we evaluated how magnetic targeting could affect the accumulation of Fe_3O_4@$HSiO_2$–COLC around tumor cells (illustrated in **Figure 8**g). First, different magnetic fields were chosen at 0.05, 0.15, and 0.5 Tesla. It was found to be magnetic-field-dependent as shown in Figure 7, when not subjected to the external

magnetic field, Fe_3O_4@$HSiO_2$–COLC nanoparticles were dispersed uniformly around cells (Figure 8a–c). However, when subjected to different external magnetic field, different proportions of Fe_3O_4@$HSiO_2$–COLC nanoparticles were accumulated to target place (Figure 8d–f). The higher magnetic field, especially at 0.5 Tesla, the more Fe_3O_4@$HSiO_2$–COLC nanoparticles were accumulated by magnetic force, which caused much higher cytotoxicity and more amounts of dead cell (Figure 8f). For low magnetic field at 0.05 Tesla, lower cell death ratio was observed due to lower amount of Fe_3O_4@$HSiO_2$–COLC nanoparticles (Figure 8d). These results indicated that high magnetic field was beneficial to delivery Fe_3O_4@$HSiO_2$–COLC nanomedicine into target tissue. Therefore, Fe_3O_4@$HSiO_2$–COLC core–shell nanoparticles possessed good potential as a new targeted drug delivery system for cancer therapy.

3. Conclusions

A multifunctional material (Fe_3O_4@$HSiO_2$) as an MR contrast agent and a drug delivery system has been successfully developed. The porous Fe_3O_4@$HSiO_2$ possessed uniform shape, narrow PSD, and acid degradation activity. Meanwhile, the porous Fe_3O_4@$HSiO_2$ showed high loading capacity for COLC due to hydrogen bond interaction and van der Waals force, and well targeted due to high magnetic field interaction. The loaded COLC could be easily released for chemotherapy, since the microenvironment of tumors is acidic. MR relaxation enhancement effects of Fe_3O_4@$HSiO_2$ core–shell nanoparticles in acid SBF could provide a direct method to detect tumor tissue. Therefore, the porous Fe_3O_4@$HSiO_2$ could target a specific tumor tissue, deliver anticancer drug, and monitor the variation of the tumor by MRI. The toxicity assay on porous Fe_3O_4@$HSiO_2$ nanoparticles towards HepG2 cells showed excellent biocompatibility of Fe_3O_4@$HSiO_2$. After loading anticancer drug COLC, porous Fe_3O_4@$HSiO_2$–COLC showed well growth inhibition on HepG2 cells. Moreover, Fe_3O_4@$HSiO_2$–COLC under magnetic field exhibited much stronger growth inhibition on HepG2 cells than that under zero magnetic field.

4. Experimental Section

Materials: All chemical reagents are used as received without further purification. Ferric acetylacetonate ($Fe(acac)_3$, 98% purity), ethylene glycol (99%), and diethylene glycol (99%) were purchased from Sinopharm Chemical Reagent Co., Ltd. (Shanghai, China). Colchicine (99%), TEOS (99.99%), and sodium borohydride (96%) were provided by Aladdin Chemistry Co. Ltd. (Shanghai, China). Polyvinylpyrrolidone (PVP-K30) of analytical reagent grade was purchased from Fluka-Solarbio (Beijing, China). Human hepatoma cells (HepG2-cells) were purchased from Chinese Academy of Medical Sciences Tumor Cell Culture.

Synthesis of Fe_3O_4 Particles: First, 0.5 g $Fe(acac)_3$ was dissolved in the mixed solution of 20 mL ethylene glycol and 30 mL diethylene glycol. Then,1.5 g PVP-K30 was dissolved in the solution. The resulting solution was placed at 120 °C for 60 min to form a homogeneous solution. 2 g NaOAc was added into the homogeneous solution and stirred at room temperature for 30 min. After that, the obtained solution was transferred to teflon-lined stainless steel autoclaves and kept at 200 °C for 12 h. Finally, the black product was dried in vacuum drying oven after being washed with distilled water and alcohol for at least three times.

Synthesis of Fe_3O_4@SiO_2 Nanospheres: The core–shell Fe_3O_4@SiO_2 nanospheres were synthesized as previously described. Briefly, 0.1 g Fe_3O_4 nanoparticles (approximately 100 nm in diameter) were dispersed in the mixed solution of 140 mL ethanol, 20 mL distilled water, and 2 mL stronger ammonia water (28 %) by ultrasonication for 15 min to form a colloidal solution. Afterwards, the mixed solution of 1.5 mL TEOS and 10 mL ethanol was added to the resulting solution drop by drop. After stirring at room temperature for about 30 h, the product (actually Fe_3O_4@SiO_2 nanospheres) was collected with a magnet and dried at 50 °C in vacuum drying oven after being washed with distilled water and ethanol for three times.

Preparation of Functional Porous Fe_3O_4@$HSiO_2$: 0.1 g Fe_3O_4@SiO_2 was dispersed in 20 mL distilled water and the resulting suspension was added to 10 mL sodium borohydride solution (8 g L^{-1}) at 0 °C. The obtained suspension was transferred to teflon-lined stainless steel autoclaves and kept 80 °C for 12 h. The product (actually the Fe_3O_4@$HSiO_2$ nanospheres) was collected with a magnet and dried at 30 °C in vacuum drying oven after being washed with acetone, ethanol, and distilled water for three times.

Drug Loading and Release: 2 mg functional porous Fe_3O_4@$HSiO_2$ nanospheres were dispersed in 2 mL COLC solution (2.5 mg mL^{-1}) at pH 9.0 by shaking at ambient temperature for 24 h, making COLC loaded in Fe_3O_4@$HSiO_2$, and such complex was designated as Fe_3O_4@$HSiO_2$–COLC. After centrifuging at 15 000 r min^{-1} for 10 min, the Fe_3O_4@$HSiO_2$–COLC precipitation was dried in vacuum drying oven. Then, 2 mg Fe_3O_4@$HSiO_2$-COLC was dispersed in 2 mL SBF by shaking for 12 h at various pH values from 3.0 to 7.4. The COLC concentration in the supernatant after centrifuging was determined using a UV–Vis spectrophotometer (UV 2550, Shimadzu Co., Japan) at wavelength of 244 or 350 nm to get the release performance.

MR Experiment: For MRI, the capability of nanospheres to influence the T_2 relaxation time was studied using a 9.4 Tesla 8.9 cm wide bore, actively screened, vertical bore MR spectrometer (Bruker Biospoin GmbH, Germany). The transverse relaxation (T_2) rates were measured using a multi-echo spin echo sequence with repetition time (TR) of 2500 ms and 20 echoes with echo times (TE) ranging from 10 to 200 ms. The T_2 relaxivity (r_2) was determined by a linear fit of the inverse relaxation times as a function of the iron concentration, which was determined using a UV–Vis spectrophotometer (UV 2550, Shimadzu Co., Japan) at wavelength of 510 nm.

In Vitro Magnetic Resonance Imaging: HepG2 cells were cultured in Dulbecco's modified eagle medium (DMEM)/high-glucose medium (Hyclone, China) supplemented with 10% (v/v) heat-inactivated fetal bovine serum and 1% penicillin–streptomycin at 37 °C in a humidified atmosphere with 5% CO_2. Prior to the treatment, HepG2 cells were adjusted to a density of 5×10^5 cells/dish (60 mm diameter). Then cells incubated with 0, 10, 20, 40, and 60 μg mL^{-1} of H^+-Fe_3O_4@$HSiO_2$ nanoparticles were subjected to magnetic field at 0.5 Tesla and non-magnetic field. After a treatment for 1 h, media were removed, then cells were harvested, suspended, and fixed in 1.2 mL of PBS:2% paraformaldehyde (1:1, v/v) at 4 °C for 1 h. Cells were centrifuged to remove paraformaldehyde at 800 rpm for 2 min, washed twice with PBS, resuspended in 50 μL PBS, and finally 150 μL of 0.8% agarose solutions were added onto cells. The mixture was carefully transferred into 5 mm NMR tube. Cells treated with four concentrations of iron (0, 20, 40, and 60 μg mL^{-1}) were chosen and scanned under a 9.4 T MR spectrometer at room temperature, and signal intensity of each NMR tube was plotted in Figure 6b.

In Vitro Cytotoxicity and Cell Viability Study: The in vitro cytotoxicities of free COLC, Fe_3O_4@$HSiO_2$, and Fe_3O_4@$HSiO_2$–COLC were assessed on HepG2 cells using the Cell Counting Kit-8 (CCK-8) method. For treatment, cells were cultured in different multi-well dishes depending on the respective experiment at a density of either 1×10^4 cells/well in 250 μL (96-well) or 2×10^5 cells/well in 2 mL (30 mm diameter) of complete medium. After 24 h, medium was removed and cells were incubated with the different samples containing free COLC, Fe_3O_4@$HSiO_2$, and Fe_3O_4@$HSiO_2$–COLC. Within all experiments, five different concentrations (10, 20, 40, 60, and 80 μg mL^{-1}) and an incubation

period of 24, 48, 72, and 96 h were considered under the action of the presence (HepG2 cells were placed on 0.5 Tesla magnet) and absence of magnetic field. In addition, to investigate different magnetic fields effect on nanomedicine, HepG2 cells, treated with Fe_3O_4@$HSiO_2$–COLC nanoparticles (40 μg mL^{-1}), were placed under three different magnetic fields (0.05, 0.15, and 0.5 Tesla) for 24 h. For delivery to the cells, all compounds were dissolved in a basic medium. Equivalent quantities of basic medium were added to control cells. After incubation, both floating and attached cells were collected for analysis. The morphological changes of cells were observed by fluorescent microscope (OLYMPUS TH4-200).

Characterization: The morphology and microstructure were observed on a scanning electron microscope (SEM) (Sirion 200, FEI Co., USA) and an H-800 transmission electron microscope (TEM) (Hitachi Co., Japan). The nitrogen adsorption–desorption isotherm was measured using a porosimetry analyzer (Tristar II, 3020M, Micromeritics, USA). The particle size distribution was determined by a DLS detector (Malvern, UK). The zeta potential was measured by zetasizer 3000 (Malvern, UK). The structure and interaction were analyzed using a Fourier transform infrared spectrometer (Bruker Co., Germany) and a proton magnetic resonance spectrometer (Bruker Co., Germany).

Supporting Information

Supporting Information is available from the Wiley Online Library or from the author.

Acknowledgements

This work was supported by the National Natural Science Foundation of China (No. 10975154, No. 21072002, No. U1232212) and Scientific and Technological Project of Anhui Province (No. 1206c0805014).

Received: November 21, 2013
Revised: February 21, 2014
Published online: April 1, 2014

[1] K. N. Sugahara, T. Teesalu, P. P. Karmali, V. R. Kotamraju, L. Agemy, D. R. Greenwald, E. Ruoslahti, *Science* **2010**, *328*, 1031.
[2] D. Ghosh, Y. Lee, S. Thomas, A. G. Kohli, D. S. Yun, A. M. Belcher, K. A. Kelly, *Nat. Nanotechnol.* **2012**, *146*, 1.
[3] F. Zhang, G. B. Braun, A. Pallaoro, Y. C. Zhang, Y. F. Shi, *Nano Lett.* **2012**, *12*, 61.
[4] J. Y. Kim, S. G. Park, J. E. Lee, S. M. Jin, J. H. Lee, I. S. Lee, I. L. Yang, J. S. Kim, S. K. Kim, M. H. Cho, T. H. Hyeon, *Angew. Chem. Int. Ed.* **2006**, *45*, 7754.
[5] J. Y. Kim, H. S. Kim, N. Lee, T. Kim, H. Kim, T. Yu, I. C. Song, W. K. Moon, T. H. Hyeon, *Angew. Chem. Int. Ed.* **2008**, *47*, 8438.
[6] N. Insin, J. B. Tracy, H. Lee, J. P. Zimmer, R. M. Westervelt, M. G. Bawendi, *ACS Nano* **2008**, *2*, 197.
[7] S. Gai, P. Yang, C. Li, W. Wang, Y. Dai, N. Niu, J. Lin, *Adv. Funct. Mater.* **2010**, *20*, 1166.
[8] D. H. Liu, F. X. Liu, Z. H. Liu, L. L. Wang, N. Zhang, *Mol. Pharm.* **2011**, *8*, 2291.
[9] K. Cheng, S. Peng, C. J. Xu, S. H. Sun, *J. Am. Chem. Soc.* **2009**, *131*, 10637.
[10] X. J. Kang, Y. L. Dai, P. A. Ma, D. M. Yang, C. X. Li, Z. Y. Hou, Z. Y. Cheng, J. Lin, *Chem. Eur. J.* **2012**, *18*, 15676.
[11] Y. X. Wang, S. M. Hussain, G. P. Krestin, *Eur. Radiol.* **2001**, *11*, 2319.
[12] J. A. Hubbell, A. Chilkoti, *Science* **2012**, *337*, 303.
[13] E. Gullotti, Y. Yeo, *Mol. Pharm.* **2009**, *6*, 1041.
[14] Y. Liu, W. Zhang, T. J. Pinnavaia, *Angew. Chem. Int. Ed.* **2001**, *40*, 1255.
[15] Y. Han, D. Li, L. Zhao, F. S. Xiao, *Angew. Chem. Int. Ed.* **2003**, *42*, 3633.
[16] D. R. Radu, C. Y. Lai, K. Jeftinija, E. W. Rowe, S. Jeftinija, V. S. Y. Lin, *J. Am. Chem. Soc.* **2004**, *126*, 13216.
[17] X. J. Kang, Z. Y. Cheng, D. M. Yang, J. Lin, *Adv. Funct. Mater.* **2012**, *22*, 1470.
[18] Q. Yang, S. C. Wang, P. W. Fan, F. S. Xiao, Y. Di, K. F. Lin, *Chem. Mater.* **2005**, *17*, 5999.
[19] N. K. Mal, M. Fujiwara, Y. Tanaka, *Nature* **2003**, *421*, 350.
[20] N. K. Mal, M. Fujiwara, Y. Tanaka, T. Taguchi, M. Matsukata, *Chem. Mater.* **2003**, *15*, 3385.
[21] D. L. J. Thorek, A. Tsourkas, *Biomaterials* **2008**, *29*, 3583.
[22] S. H. Xuan, F. Wang, J. M. Y. Lai, K. W. Y. Sham, Y.-X. J. Wang, S. F. Lee, J. C. Yu, C. H. K Cheng, K. C. F. Leung, *ACS Appl. Mater. Interfaces* **2011**, *3*, 237.
[23] W. L. Chiang, C. J. Ke, Z. X. Liao, S. Y. Chen, F. R. Chen, C. Y. Tsai, Y. Xia, H. W. Sung, *Small* **2012**, *8*, 3584.
[24] A. Hatefi, B. Amsden, *J. Controlled Release* **2002**, *80*, 9.
[25] S. Abdul, S. S. Poddar, *J. Controlled Release* **2004**, *97*, 393.
[26] H. Ai, C. Flask, B. Weinberg, X. T. Shuai, M. D. Pagel, D. Farrell, J. Duerk, J. M. Gao, *Adv. Mater.* **2005**, *17*, 1749.
[27] N. Nasongkla, E. Bey, J. M. Ren, H. Ai, C. Khemtong, J. S. Guthi, S. F. Chin, A. D. Sherry, D. A. Boothman, J. M. Gao, *Nano Lett.* **2006**, *6*, 2427.
[28] Y. Chen, H. R. Chen, D. P. Zeng, Y. B. Tian, F. Chen, J. W. Fen, J. L. Shi, *ACS Nano* **2010**, *4*, 6001.
[29] Y. F. Zhu, Y. Fang, S. Kaskel, *J. Phys. Chem. C.* **2010**, *114*, 16382.
[30] H. M. Chen, C. H. Deng, X. M. Zhang, *Angew. Chem. Int. Ed.* **2010**, *49*, 607.
[31] W. Stober, A. Fink, E. Bohn, *J. Colloid Interface Sci.* **1968**, *26*, 62.
[32] Q. M. Ji, C. Y. Guo, X. Y. Yu, C. J. Ochs, J. P. Hill, F. Caruso, H. Nakazawa, K. Ariga, *Small* **2012**, *8*, 2345.
[33] Z. S. Chao, T. H. Wu, J. L. Ye, G. Z. Chen, H. L. Wan, *Sci. China* **2001**, *44*, 103.
[34] J. P. Ge, Y. X. Hu, M. Biasini, W. P. Beyermann, Y. D. Yin, *Angew. Chem. Int. Ed.* **2007**, *46*, 4342.
[35] J. H. Gao, G. L. Liang, J. S. Cheung, Y. Pan, Y. Kuang, F. Zhao, B. Zhang, X. X. Zhang, E. X. Wu, B. Xu, *J. Am. Chem. Soc.* **2008**, *130*, 11828.
[36] E. A. Schellenberger, D. Sosnovik, R. Weissleder, L. Josephson, *Bioconjugate. Chem.* **2004**, *15*, 1062.
[37] X. B. Fan, J. N. River, M. Zamora, K. Tarlo, K. Kellar, C. R. Schaeffer, G. S. Karczma, *Magn. Reson. Med.* **2001**, *45*, 1046.
[38] T. Shen, R. Weissleder, M. Papisov, A. J. Bogdanov, T. J. Brady, *Magn. Reson. Med.* **1993**, *29*, 599.